Responses of Different Nonhydrostatic, Pressure-Coordinate Models to Orographic Forcing

R. RÕÕM

Tartu Observatory, Toravere, Estonia

A. MÄNNIK

Tartu University, Tartu, Estonia

(Manuscript received 28 January 1998, in final form 24 September 1998)

ABSTRACT

Estimation of accuracy of different high-resolution, sound-filtered, pressure-coordinate models is carried out by modeling their response to orographic forcing. Evaluated models are the elastic nonhydrostatic model (EFM), the anelastic nonhydrostatic model (AEM), and the hydrostatic primitive equation model (HSM). These models are compared to the exact, nonfiltered, nonhydrostatic, pressure-coordinate dynamics (ExM). All model equations are linearized, a wave equation for vertical displacements of air particles is derived, and exact analytical stationary solutions for each model are compared for uniform flow over given smooth orography (bell-shaped mountain). These linear solutions reveal that compressible (ExM, EFM) and incompressible (AEM, HSM) models are different at long horizontal scales $l \sim 1000$ km. Differences are especially large in the vertical velocity field (up to 100%) at the medium and upper levels of the atmosphere, where incompressible models give systematic reductions of wave amplitudes. All models are effectively incompressible and coincide with high precision in the region 10 km $< l <$ 500–700 km. As expected, the first critical scale is $l \sim 10$ km, below which the HSM fails. The second critical scale is at $l \sim 100$ m (moderate winds) to $l \sim 1000$ m (strong winds), below which the AEM becomes inconsistent with the other models in temperature fluctuation presentation. The EFM represents a universal approximation, valid at all scales.

1. Introduction

The use of the pressure as the vertical coordinate in atmospheric dynamics was proposed by Eliassen (1949) for the hydrostatic primitive equation model (HSM), for which the hydrostatic (HS) equation

$$\frac{\partial p}{\partial z} = -g\rho,$$

where p is pressure, g is gravity, and ρ is density. Still, a transformation of dynamical equations from ordinary Cartesian coordinates $\{x, y, z\}$ to the pressure coordinates $\{x, y, p\}$ (pressure or p space) does not require the HS assumption at all, but is correct so far as pressure is a monotone function of the height,

$$\frac{\partial p}{\partial z} < 0,$$

everywhere in the modeling domain (Rõõm 1989). An inspection of the vertical development equation

$$\rho\frac{dw}{dt} = -g\rho - \frac{\partial p}{\partial z}$$

reveals that this takes place if the vertical acceleration dw/dt is either positive or, in the negative case, does not exceed the free-fall acceleration g by absolute value:

$$\frac{dw}{dt} > -g.$$

Thus, the p-space concept is quite broad and applicable almost everywhere in atmospheric dynamics, except fast energetic processes like explosions and short-scale acoustic oscillations of very large amplitude. This generality along with important applications in mesoscale modeling and nonhydrostatic (NH) weather forecast models makes pressure-space attractive for numerical modeling applications.

There exist several filtered NH, p-space models that have been successfully employed in numerical modeling. The first NH model in pressure coordinates was developed by Miller and Pearce (1974), and generalized

Corresponding author address: Dr. Rein Rõõm, Tartu Observatory, EE2444 Tartumaa, Toravere, Estonia.
E-mail: room@aai.ee

by White (1989) and Salmon and Smith (1994). The Miller and Pearce (1974) model has been employed by Xue and Thorpe (1991), Miranda and James (1992), Miranda and Valente (1997), and Rõõm (1997). A model that employs the HS component of the pressure field as a vertical coordinate was developed by Laprise (1992), and it is used in the Météo-France model ALADIN (Bubnova et al. 1995).

The Miller and Pearce model, as well as its generalizations by White (1989) and Salmon and Smith (1994), are anelastic *p*-space models (AEMs), as they employ the incompressibility condition of the pressure-space for acoustic filtration. The most general *p*-space model of atmospheric dynamics (the ''exact model,'' or ExM further), which does not make any simplification in basic primitive equations and includes, besides the NH component, the acoustical mode as well, was developed by Rõõm (1989, 1990). On the basis of this general model, a sound-filtered pressure-space model was recently proposed by Rõõm and Ülejõe (1996), and an extended version by Rõõm (1998), which employs the infinite sound speed for acoustic filtration rather than the *p*-space volume preservation. Due to the infinite sound speed, the wave equation for NH geopotential height is replaced by a Poisson equation, and the geopotential height is treated as a quasi-statically (but not hydrostatically) balanced quantity. In this model the medium is weakly compressible in the *p* space, though acoustic waves are not supported. For this reason we call this model the elastic filtered model (EFM).

The EFM was developed using scale analysis arguments and has never been numerically tested. Thus, it not is clear what advantages, if any, it has in comparison with the common anelastic models. Such an investigation is carried out in the present work. Actually, the anelastic *p*-space models lack such verification, too. Though there exist numerous tests in the mesoscale domain 10–100 km (Xue and Thorpe 1991; Miranda and James 1992), the AEMs were tested neither at shorter nor at longer scales. For this reason we will test the AEM simultaneously with the EFM. And finally, an object for mutual testing is the HS primitive equation model (HSM), which represents the long-wave asymptote of the AEM. These three filtered models are compared with the ExM. Testing compares the linear response of different models to orographic forcing. First, all model equations are linearized; the wave equations for vertical displacements of material particles are derived. Then, exact analytical solutions for uniform flow over given smooth orography (bell-shaped mountain) are presented. Finally, solutions of filtered models are compared to the corresponding solution of the ExM.

This paper is analogous to the first, linear part of the investigation by Nance and Durran (1994), who carried out a comparison of four different sound-relaxed (''sound-proof'' according to their terminology) models in common space.

2. Dynamical *p*-space models

a. Exact, nonfiltered model

The ExM (Rõõm 1989, 1990, 1998) reads

$$\frac{dz}{dt} = w, \tag{1a}$$

$$n\frac{dw}{dt} = g(1 - n), \tag{1b}$$

$$n\frac{d\mathbf{v}}{dt} = -g\boldsymbol{\nabla}z - nf\mathbf{k} \times \mathbf{v}, \tag{1c}$$

$$\frac{dT}{dt} = \frac{RT\omega}{c_p p} + Q, \tag{1d}$$

$$\frac{dn}{dt} = -n(\boldsymbol{\nabla} \cdot \mathbf{v} + \partial\omega/\partial p), \tag{1e}$$

$$n = -\frac{p}{H}\frac{\partial z}{\partial p}. \tag{1f}$$

Here, $z(x, y, p, t)$ represents the NH geopotential height of the air particle above sea level; $\mathbf{v} = (u, v)$ and w are horizontal wind vector and vertical wind, respectively; $\omega = dp/dt$ represents the omega velocity of an air particle; n is the normalized, nondimensional density in pressure coordinates, which is related to the ordinary air density by

$$n\ \delta p = g\rho\ \delta z,$$

where δp and δz represent vertical extents of an infinitesimal air particle; Q is the thermal forcing (heat source divided by specific heat at constant pressure, c_p); p_0 presents the surface pressure; $\mathbf{k}$ represents the vertical unit vector; and

$$H = RT/g$$

is the scale height. The total (or Lagrangian) derivative is defined as

$$\frac{d}{dt} = \frac{\partial}{\partial t} + \mathbf{v} \cdot \boldsymbol{\nabla} + \omega\frac{\partial}{\partial p}.$$

Equation (1f) represents a generalization of HS relation $n = 1$ to the NH case. The omega velocity ω is a diagnostic variable, and the explicit equation for this quantity can be derived by differentiating (1f) in time:

$$\alpha\frac{\omega}{p} = \frac{p}{nH}\left(\frac{\partial w}{\partial p} - \frac{\partial \mathbf{v}}{\partial p} \cdot \boldsymbol{\nabla}z\right) - \boldsymbol{\nabla} \cdot \mathbf{v} + \frac{Q}{T}, \tag{1g}$$

where $\alpha = c_v/c_p$.

b. Anelastic p-space models

Anelastic *p*-space models are the ones for which the *p*-space density n is constant and coincides with its HS value $n = 1$ in the continuity equation [(1e)], yielding nondivergence of velocity, $\boldsymbol{\nabla} \cdot \mathbf{v} + \partial\omega/\partial p = 0$. Known anelastic *p*-space models are the Miller and Pearce mod-

el (Miller and Pearce 1974), the White model (White 1989), and the Salmon and Smith model (Salmon and Smith 1994). The most general one is the Salmon and Smith model, which supports arbitrary thermodynamics. The White model assumes a thermodynamically perfect atmosphere. Particularly, these two models coincide for perfect gas in the absence of heat sources. The Miller and Pearce model is close to the White model but assumes in addition a partial linearization in the right-hand sides of vertical development and temperature equations in respect to the hydrostatic background state of the atmosphere. All three models coincide in the linear adiabatic case. Keeping in mind the close relationship of three models, we will choose the White model to the representative of anelastic *p*-space models.

The White model can be obtained from (1), using incompressibility approximation $n = 1$ everywhere except the right side of Eq. (1b), along with the approximation for vertical velocity

$$w = \frac{dz}{dt} \approx \omega \frac{\partial z_s}{\partial p} = -H\frac{\omega}{p}.$$

The resulting model equations are

$$w = -H\frac{\omega}{p}, \tag{2a}$$

$$\frac{dw}{dt} = g\left(1 + \frac{p}{H}\frac{\partial z}{\partial p}\right), \tag{2b}$$

$$\frac{d\mathbf{v}}{dt} = -g\nabla z - f\mathbf{k} \times \mathbf{v}, \tag{2c}$$

$$\frac{dT}{dt} = -\frac{g}{c_p}w + Q, \tag{2d}$$

$$\nabla \cdot \mathbf{v} + \partial\omega/\partial p = 0. \tag{2e}$$

c. Hydrostatic primitive equation model

The HSM follows from the exact model [(1)], if assumption $n = 1$ is made everywhere {including the right side of the vertical development equation [(1b)]}. At the same time, the HSM represents the long-scale asymptote of the AEM at $dw/dt \to 0$ in Eq. (2b). Using this approximation, and after elimination of w from (2d) with the help of (2a), the resulting equations are

$$1 + \frac{p}{H}\frac{\partial z}{\partial p} = 0, \tag{3a}$$

$$\frac{d\mathbf{v}}{dt} = -g\nabla z - f\mathbf{k} \times \mathbf{v}, \tag{3b}$$

$$\frac{dT}{dt} = \frac{R}{c_p}\frac{\omega T}{p} + Q, \tag{3c}$$

$$\nabla \cdot \mathbf{v} + \partial\omega/\partial p = 0, \tag{3d}$$

which represent the standard form of the HSM.

d. Elastic filtered p-space model

The EFM, first presented by Rõõm and Ülejõe (1996), is deduced in an extended version from the Hamiltonian Principle by Rõõm (1998). Rather than anelasticity of pressure-space, it employs the infinitely high sound speed approximation (i.e., the zero Mach number approximation) for acoustic filtration. The EFM assumes representation

$$T = T_0(x, y, p) + T'(x, y, p, t),$$

$$z = z_0(x, y, p) + z'(x, y, p, t),$$

where $T_0(x, y, p)$ and $z_0(x, y, p)$ are appropriately chosen (for instance, climatological or seasonal mean) background fields and treats in the role of main thermodynamic variables the relative geopotential height fluctuation ζ and the relative entropy fluctuation η:

$$\zeta = \frac{z'}{H_0}, \qquad \eta = \frac{T'}{T_0} - \frac{N^2}{g}z', \tag{4}$$

where the scale height H_0 and the buoyancy frequency N of the undisturbed atmosphere are

$$H_0 = \frac{RT_0}{g}, \qquad N = \sqrt{\frac{g}{H_0}\left(\frac{R}{c_p} - \frac{p}{T_0}\frac{\partial T_0}{\partial p}\right)}. \tag{5}$$

The EFM equations are the entropy equation

$$n\frac{d}{dt}\eta = -\frac{N^2}{g}w + n\frac{Q}{T_0}; \tag{6a}$$

the vertical development equation

$$\frac{dw}{dt} = g(\hat{P}^-\zeta + \eta) - \left(w - \frac{gQ}{N^2T_0}\right)\frac{d}{dt}\ln(1 - f^2/N^2); \tag{6b}$$

the diagnostic equation for geopotential height fluctuation

$$H_0^2(\nabla \cdot n\nabla - nf^2/c_a^2)\zeta + \hat{P}^+\{n[\hat{P}^-\zeta + (1 - f^2/N^2)\eta]\} = -n\left(\frac{R}{g^2}\frac{dQ}{dt} + \frac{fH_0}{g}q\right); \tag{6c}$$

the potential vorticity equation

$$\frac{dq}{dt} = fR\frac{\partial}{\partial p}\frac{pQ}{H_0^2N^2}, \tag{6d}$$

where potential vorticity is

$$q = -\mathbf{k} \cdot (\nabla \times \mathbf{v}) + \alpha f\zeta + \frac{fg}{H_0}\hat{P}^+\frac{\eta}{N^2};$$

the continuity equation

$$\frac{dn}{dt} = -n(\nabla \cdot \mathbf{v} + \partial\omega/\partial p); \tag{6e}$$

and diagnostic equations for ω velocity and horizontal wind vector $\mathbf{v}$

$$\frac{\omega}{p} = -\frac{w}{H_0}, \tag{6f}$$

$$\mathbf{v} = \mathbf{k} \times \nabla\psi + \nabla\varphi, \tag{6g}$$

$$\nabla^2\psi = -q + \alpha f\zeta + \frac{fg}{H_0}\hat{P}^+\frac{\eta}{N^2}, \tag{6h}$$

$$\nabla^2\varphi = \frac{1}{H_0}\hat{P}^+ w + \frac{Q}{T_0}, \tag{6i}$$

where ψ and φ are the streamfunction and velocity potential, respectively. Sound speed $c_a = \sqrt{RT_0/\alpha}$, and $\hat{P}^+$, $\hat{P}^-$ are short notations for the operators

$$\hat{P}^- = \frac{\partial}{\partial p}p - \alpha, \qquad \hat{P}^+ = p\frac{\partial}{\partial p} + \alpha.$$

Because system (6) represents a compressible model, it includes the density n and density equation [(6e)]. Due to this compressibility, this model is more complicated and looks less attractive in comparison to the anelastic model. Nevertheless, it is deduced in a way that should enable optimal acoustic filtration and higher accuracy in comparison to anelastic models. Whether and when this occurs will be the main topic of the present study.

3. Stationary, linear response of filtered models to the orographic forcing

a. Linear wave equations

Our aim is to compare the above-described models using solutions to their corresponding linearized equations. This is straightforward if the problem is reduced to the investigation of corresponding linear wave equations for vertical displacements of air particles. The basic background flow state is described by relations

$$z = z_0(p), \quad T = T_0(p), \quad \mathbf{v} = \mathbf{i}U, \quad w = 0, \quad n = 1.$$

Note that the undisturbed background flow has the constant velocity U. Linearization according to this background state yields, after some algebraic manipulation (Rõõm 1997), and assuming the absence of heat sources,

$$Q = 0,$$

a scalar wave equation of the same appearance for all models

$$\hat{M}a = 0. \tag{7a}$$

Here $a(x, p)$, which is defined with the help of relation

$$w = \frac{d_0 a}{dt} \equiv \left(\frac{\partial}{\partial t} + U\frac{\partial}{\partial x}\right)a, \tag{7b}$$

represents vertical displacement of an individual air particle. The operator $\hat{M}$ for each model is

$$\text{ExM}, \quad \hat{M} = \left(\frac{d_0^2}{dt^2} + N^2\right)\left[\nabla^2 - \frac{1}{c_a^2}\left(\frac{d_0^2}{dt^2} + f^2\right)\right] + \left(\frac{d_0^2}{dt^2} + f^2\right)\hat{P}^-\frac{1}{H_0^2}\hat{P}^+; \tag{8a}$$

$$\text{EFM}, \quad \hat{M} = \left(\frac{d_0^2}{dt^2} + N^2\right)\left(\nabla^2 - \frac{f^2}{c_a^2}\right) + \left(\frac{d_0^2}{dt^2} + f^2\right)\hat{P}^-\frac{1}{H_0^2}\hat{P}^+; \tag{8b}$$

$$\text{AEM}, \quad \hat{M} = \left(\frac{d_0^2}{dt^2} + N^2\right)\nabla^2 + \left(\frac{d_0^2}{dt^2} + f^2\right)\frac{p}{H_0}\frac{\partial^2}{\partial p^2}\frac{p}{H_0}; \tag{8c}$$

$$\text{HSM}, \quad \hat{M} = N^2\nabla^2 + \left(\frac{d_0^2}{dt^2} + f^2\right)\frac{p}{H_0}\frac{\partial^2}{\partial p^2}\frac{p}{H_0}. \tag{8d}$$

As it appears from these representations, the EFM represents a slow asymptote of the ExM, valid for flows that satisfy condition $(1/c_a)^2 d_0^2/dt^2 a \ll \nabla^2 a$, whereas the AEM transforms to the HSM for slow and horizontally long-scale flow regimes for which $d_0^2/dt^2 a \ll N^2 a$.

Equation (7a) is solved in stationary case (a does not depend on t) in two-dimensional geometry in the rectangular domain

$$-L \le x \le L, \qquad 0 < p \le p_s, \tag{9}$$

where $p_s = 1000$ mb is the constant sea level pressure. Orography and solution are considered independent of the y coordinate. The basic case that is studied is the stationary response of the atmosphere to orographic forcing:

$$w(x, p_s) = [U + u(x, p_s)]\frac{\partial h}{\partial x}, \tag{10}$$

where $u(x, p)$ represents the disturbance of horizontal velocity, and $h(x)$ is the orography function, which in most examples is modeled by the bell-shaped isolated mountain, the so-called Witch of Agnesi:

$$h(x) = \frac{h_0}{1 + x^2/l^2}, \tag{11}$$

with the maximum height h_0 and half-width l. A simpler boundary condition,

$$w(x, p_s) = U\frac{\partial h}{\partial x},$$

was applied in an earlier paper (Rõõm 1997). This condition assumes a low, not steep, mountain profile and

yields systematic distortions for high or steep mountains, which manifest themselves in the intersections of flow trajectories with ground surface and make interpretation of the results and comparison of different models ambiguous. For this reason the exact free-slip kinematic lower-boundary condition [(10)] is assumed in this paper.

The radiative boundary condition (Baines 1995) is applied at the top of the domain $p \to 0$. Zero boundary condition is assumed at lateral boundaries: $a(\pm L, p) = 0$, which is an approximation to the exact condition $a(\pm\infty, p) = 0$, and which can be used if $l \ll L$. Because this condition represents a special case of periodic lateral boundary conditions, it supports the application of a Fourier transform at solution.

The orographic response study has been a popular tool for model validations. Beginning with classic works by Queney (1948), Scorer (1949, 1953, 1954, 1956), Long (1953), and Alaka (1960), numerous papers have been published on the modeling of two-dimensional flows over isolated topography, both linear and nonlinear, with analytical and numerical content [see overviews by Smith (1979) and Baines (1995)]. Due to the known analytical solutions, mountain waves have been common objects for model tests (Laprise and Peltier 1989; Lin and Wang 1996; Hereil and Laprise 1996). Our examples do not represent anything new and original in this respect. Our sole purpose is model comparison. The use of well-documented examples is justified as it increases the authenticity of the results.

b. Modeled fields

In the following, the vertical velocity, the potential temperature, and the streamlines of the flow are presented as final modeling products and illustrative material. The vertical velocity is calculated from (7b). The potential temperature field is calculated according to the formula

$$\Theta(x, p) = \Theta_0(p)\left[1 + \frac{T'(x, p)}{T_0(p)}\right],$$

where the background potential temperature is the solution of the equation

$$\frac{d\Theta_0}{dp} = -\frac{H_0(p)N^2(p)}{gp}\Theta_0.$$

The temperature computation is case sensitive. In the case of ExM and EFM, η and ζ are first found from

$$\eta = -\frac{N^2}{g}a, \qquad \hat{P}^{-}\zeta = -\left(1 + \frac{1}{N^2}\frac{d_0^2}{dt^2}\right)\eta + \frac{1}{N^2}\frac{d_0}{dt}\frac{Q}{T_0}$$

(for details, see Rõõm 1997), and then temperature fluctuations are calculated from (4). In the case of AEM and HSM, the relation

$$\frac{d_0}{dt}\left(\frac{T'}{T_0} + \frac{N^2}{g}a\right) = \frac{Q}{T_0}$$

is used [follows with the help of (7b) from the linearized form of (2d)], which for $Q = 0$ simplifies to

$$\frac{T'}{T_0} = -\frac{N^2}{g}a.$$

Trajectory integration also differs from case to case. Acoustically filtered models EFM, AEM, and HSM have streamfunctions $\Psi(x, p)$, which are constant along trajectories,

$$\frac{d}{dt}\Psi = [U + u(x, p)]\frac{\partial\Psi}{\partial x} + \omega\frac{\partial\Psi}{\partial p} = 0,$$

and isolines of which are streamlines. The streamfunction for both AEM and HSM and the corresponding formulas for velocity components are

$$\Psi(x, p) = \frac{p}{p_s}\left[1 + \frac{a(x, p)}{H_0(p)}\right], \tag{12a}$$

$$U + u(x, p) = Up_s\frac{\partial\Psi}{\partial p}, \qquad \omega = -Up_s\frac{\partial\Psi}{\partial x}; \tag{12b}$$

and for the EFM,

$$\Psi(x, p) = \left(\frac{p}{p_s}\right)^{\alpha}\left[\frac{\alpha}{p^{\alpha}}\int_0^p \frac{H_0(p')}{\overline{H_0}}(p')^{\alpha-1}\,dp' + \alpha\frac{a(x,p)}{\overline{H_0}}\right], \tag{13a}$$

$$U + u(x,p) = U\frac{p_s}{\alpha}\left(\frac{p}{p_s}\right)^{1-\alpha}\frac{\partial\Psi}{\partial p},$$

$$\omega = -U\frac{p_s}{\alpha}\left(\frac{p}{p_s}\right)^{1-\alpha}\frac{\partial\Psi}{\partial x}, \tag{13b}$$

where $\overline{H_0}$ represents the vertically averaged value of $H_0(p)$. For constant $H_0 = \overline{H_0}$ Eq. (13a) reduces to

$$\text{EFM,} \quad \Psi(x, p) = \left(\frac{p}{p_s}\right)^{\alpha}\left[1 + \alpha\frac{a(x, p)}{H_0}\right]. \tag{13a$'$}$$

As it appears, in the homogeneous atmosphere with constant H_0, streamfunction for the EFM transforms to the streamfunction for the AEM formally at $\alpha \to 1$, which assumes $C_v = C_p$, and as a consequence, incompressibility of the atmosphere in the common space. In both models the streamfunction consists of the undisturbed part $\Psi_0(p)$, which is represented by the first term in (12) and (13a$'$), and of the perturbation part $\Psi'(x, p)$, proportional to $a(x, p)$.

For the ExM the streamfunction does not exist and streamlines are found as particle trajectories, integrating equations

$$\frac{dx}{dt} = U + u(x, p), \qquad \frac{dp}{dt} = \omega(x, p)$$

numerically.

c. Orographic waves on homogeneous background

This is the model of constant H_0 and N. Although there exists only one case when both the scale height and buoyancy frequency are exactly constant simultaneously—the case of constant T_0—it is widely practiced in linear modeling to treat these two parameters as independent constants. On the one hand, this model is a satisfactory approximation to the real stratification of the climatologically mean troposphere, and corresponding solutions catch the main features of real atmospheric flows; on the other hand, this is the case that can be solved analytically. Looking for the solution in the form of the Fourier series

$$a(x, p) = \frac{1}{2\pi} \sum_{\kappa} \tilde{a}_{\kappa}(p) e^{-i\kappa x},$$

where $\tilde{a}_{\kappa}(p)$ are the Fourier coefficients of a with wavenumber κ, and representing the orography function similarly

$$h(x) = \frac{1}{2\pi} \sum_{\kappa} \tilde{h}_{\kappa} e^{-i\kappa x}.$$

Equation (7a) transforms to a system of ordinary differential equations (independent for different κ) of the form

$$\left[\left(p\frac{d}{dp}\right)^2 + p\frac{d}{dp} + \frac{1}{4} + m_{\kappa}\right]\tilde{a}_{\kappa} = 0, \qquad (14)$$

where all the differences between the models are located in the coefficient m_{κ}:

$$\text{ExM}, \quad m_{\kappa} = H_0^2\kappa^2 \times \left(1 - \mathcal{M}^2 + \frac{f^2}{c_a^2\kappa^2}\right) \times \frac{N^2 - U^2\kappa^2}{U^2\kappa^2 - f^2} - \left(\alpha - \frac{1}{2}\right)^2, \qquad (15a)$$

$$\text{EFM}, \quad m_{\kappa} = H_0^2\kappa^2 \times \left(1 + \frac{f^2}{c_a^2\kappa^2}\right) \times \frac{N^2 - U^2\kappa^2}{U^2\kappa^2 - f^2} - \left(\alpha - \frac{1}{2}\right)^2, \qquad (15b)$$

$$\text{AEM}, \quad m_{\kappa} = H_0^2\kappa^2 \times \frac{N^2 - U^2\kappa^2}{U^2\kappa^2 - f^2} - \frac{1}{4}, \qquad (15c)$$

$$\text{HSM}, \quad m_{\kappa} = H_0^2\kappa^2 \times \frac{N^2}{U^2\kappa^2 - f^2} - \frac{1}{4}, \qquad (15d)$$

where $\mathcal{M} = U/c_a$ is the Mach number of the basic flow.

In numerical computations the fast Fourier transform is applied, and consequently, the infinite Fourier series are replaced by the appropriate finite discrete Fourier series, replacing simultaneously the Laplacian $\nabla^2 = \partial^2/\partial x^2$ in (8) with its discrete analogue. Such discretization yields the replacement of κ^2 in (15) by

$$\tilde{\kappa}^2 = \left[2\,\frac{\sin(\kappa\Delta x/2)}{\Delta x}\right]^2,$$

where $\Delta x = 2L/\mathcal{N}$, and $\mathcal{N}$ represents the number of the grid points on the x axis. Still, for the given l, the spectrum of the solution is effectively localized in the spectral region $\kappa \leq 2/l$ (Queney 1948). If $\Delta x \ll l$, then $\kappa\Delta x/2 \ll 1$ and $\tilde{\kappa} \approx \kappa$. Thus, the spectrum of the solution of the discrete problem matches the spectrum of the continuous solution in this case, and discretization has no effect on the quality of the solution. In further numerical examples L and $\mathcal{N}$ are always chosen to meet conditions $\Delta x \ll l \ll L$. The second inequality here guarantees that the domain of integration is large enough in the x direction to match at lateral boundaries $x = \pm L$ the exact zero condition of solution at the infinity.

The spectral dependence of m_{κ} on nondimensional wavenumber κH_0 is presented for different U and N in Fig. 1. Figure 1a represents the ExM, whereas Figs. 1b–d present relative error of m_{κ} for filtered models EFM, AEM, and HSM. As seen from Fig. 1a, m_{κ} is negative in the long-scale region, $\kappa H_0 < 0.05$, and in the short scale region, $\kappa H_0 > 5$. The regions of negative m represent the domains of the so-called trapped waves (Queney 1948; Holton 1992), which are symmetrical with respect to the vertical symmetry axis of the mountain, and there is no tilt of wave crests with height. In contrast, the region of positive m_{κ} (very approximately located in the region $0.05 < \kappa H_0 < 5$) represents the domain of so-called free waves, which have the phase shift with height (their wave crests lie on a tilted line).

As $\tilde{a}_{\kappa}$ differs essentially from zero in the spectral region $|\kappa| \leq 2/l$, the quality of the solution is mainly determined by the character of m_{κ} in this domain. At large l, the spectrum is located in the vicinity of zero. In this case, dominant features of the solution are determined by m_{κ} at $\kappa \approx 0$. With the narrowing of the width of the mountain, toward shorter l, the spectral region of the solution becomes broader and m_{κ} with larger κ will dominate. Very roughly, the quality of solution is determined by m_{κ} at $\kappa \sim 1/l$, and the comparison of m_{κ} for different models at $\kappa = 1/l$ is the prime (though not unique) source of information on model differences for flows over topography with characteristic horizontal scale l. As seen from the Fig. 1b, relative error of the EFM, $\varepsilon_{\text{EFM}} = 1 - (m_{\kappa})_{\text{AEM}}/(m_{\kappa})_{\text{ExM}}$, does not exceed 5×10^{-3} for typical atmospheric conditions. An exception is a very narrow domain in the vicinity of $\kappa H_0 \approx 5$, where $(m_{\kappa})_{\text{ExM}}$ intersects the x axis and becomes small (similar detail is apparent at the AEM, Fig. 1c). Here ε_{EFM} has a sharp spike. Still,

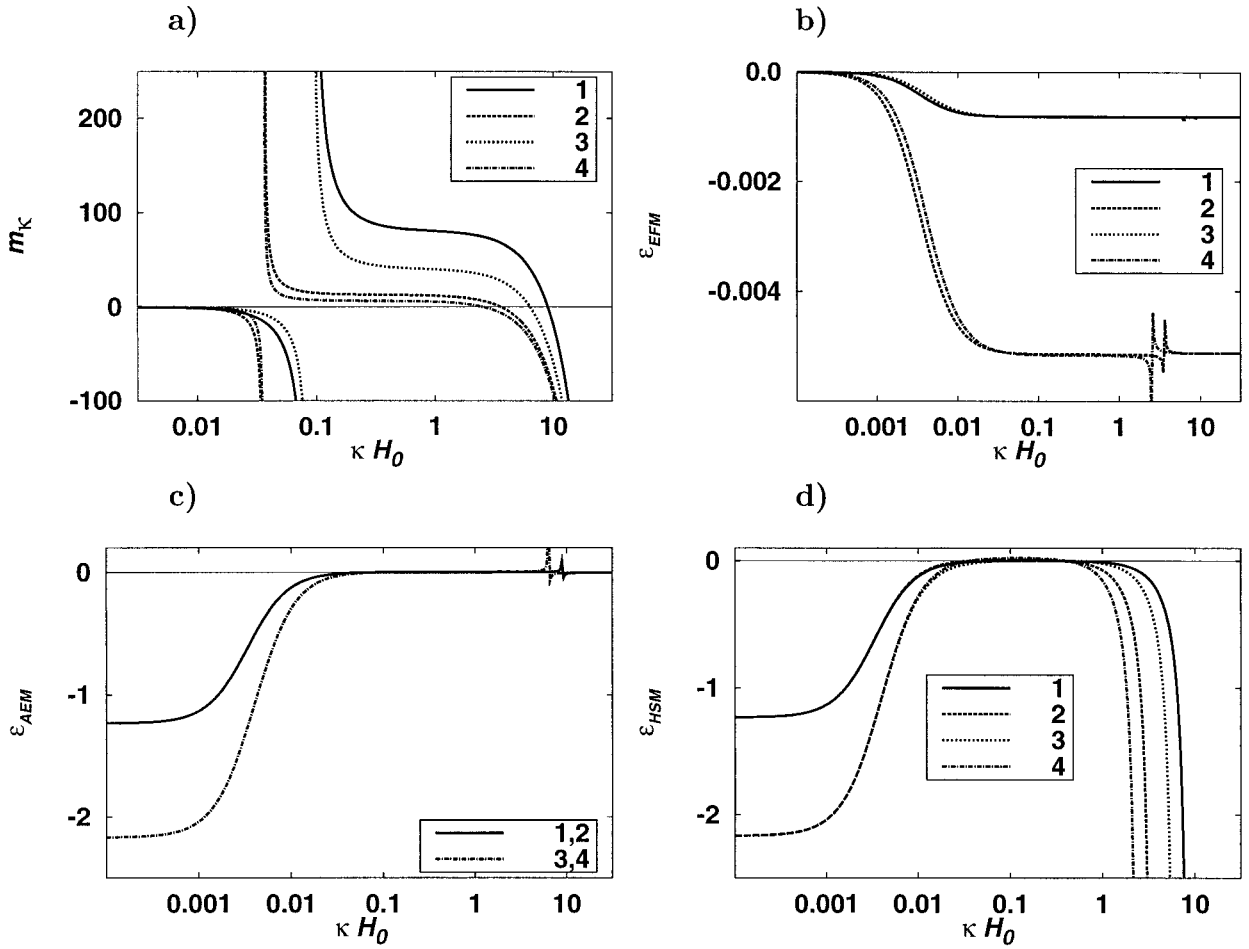

FIG. 1. Parameter m_κ as a function of the nondimensional wavenumber $H_0\kappa$ for $H_0 = 9$ km and $f = 10^{-4}$ s^{-1}. (a) Parameter m_κ of the ExM; (b), (c), (d) relative error $\varepsilon = [m - (m)_{\text{exact}}]/(m)_{\text{exact}}$ of EFM, AEM, and HSM. Curve 1, $N = 10^{-2}$ 1/s, $U = 10$ m s^{-1}; 2, $N = 10^{-2}$ 1/s, $U = 25$ m s^{-1}; 3, $N = 0.71 \times 10^{-2}$ 1/s, $U = 10$ m s^{-1}; and 4, $N = 0.71 \times 10^{-2}$ s^{-1}, $U = 25$ m s^{-1}.

as further numerical examples will demonstrate, this spike has no effect on the precision of the solution as the weight of erroneous spectral components is always small in the solution. In the case of the AEM, relative error of the m_κ is large in the long-scale region, $\kappa H_0 \leq 0.01$, and can reach at $\kappa H_0 < 0.001$ a value as large as 200% (Fig. 1c). Thus, the AEM should be most erroneous in the synoptic- and planetary-scale domain. In the case of the HSM (Fig. 1d), to this long-scale error of anelastic models a systematic error is added in the short-scale domain ($\kappa H_0 \geq 1$). This is the domain where the HSM fails.

Potential temperature wave patterns of the ExM are presented in Fig. 2 for different l and h_0 in the typical case, $H_0 = 10$ km, $N = 10^{-2}$ s^{-1}, $f = 10^{-4}$ s^{-1}, and $U = 20$ m s^{-1}. Figure 2a represents the long orography, $l = 1000$ km. As $l \gg U/f = 200$ km here, the spectrum of the solution belongs to the long-scale asymptotic domain of long trapped waves (coincides for ExM and EFM),

ExM, EFM,

$$\kappa \to 0: \quad m_\kappa \to -N^2H_0^2/c_a^2 - (\alpha - \tfrac{1}{2})^2. \qquad (16)$$

Figures 2b–d represent waves with spectra predominantly in the free-wave domain, $m_\kappa > 0$, where the wave pattern has a distinguished phase shift with the height. Figure 2b corresponds to $l = U/f = 200$ km, while $U/N \ll l \ll U/f$ for Fig. 2c, and $l = U/N = 2$ km in Fig. 2d. Figures 2e ($l = 200$ m) and 2f ($l = 20$ m) represent short-scale trapped waves with the spectrum in the domain of short-scale negative m_κ prevailingly:

$$\text{ExM}, \qquad \kappa \to \infty: \quad m_\kappa \to -(1 - \mathcal{M}^2)H_0^2\kappa^2.$$

In this short-scale nonhydrostatic domain, the sharp lift of wave crests is the result of the adiabatic air cooling near the hilltop due to the increase of the wind speed. Because computations are performed in the rectangular domain [(9)], the isolines of the potential temperature are presented below the mountain profile if they do not

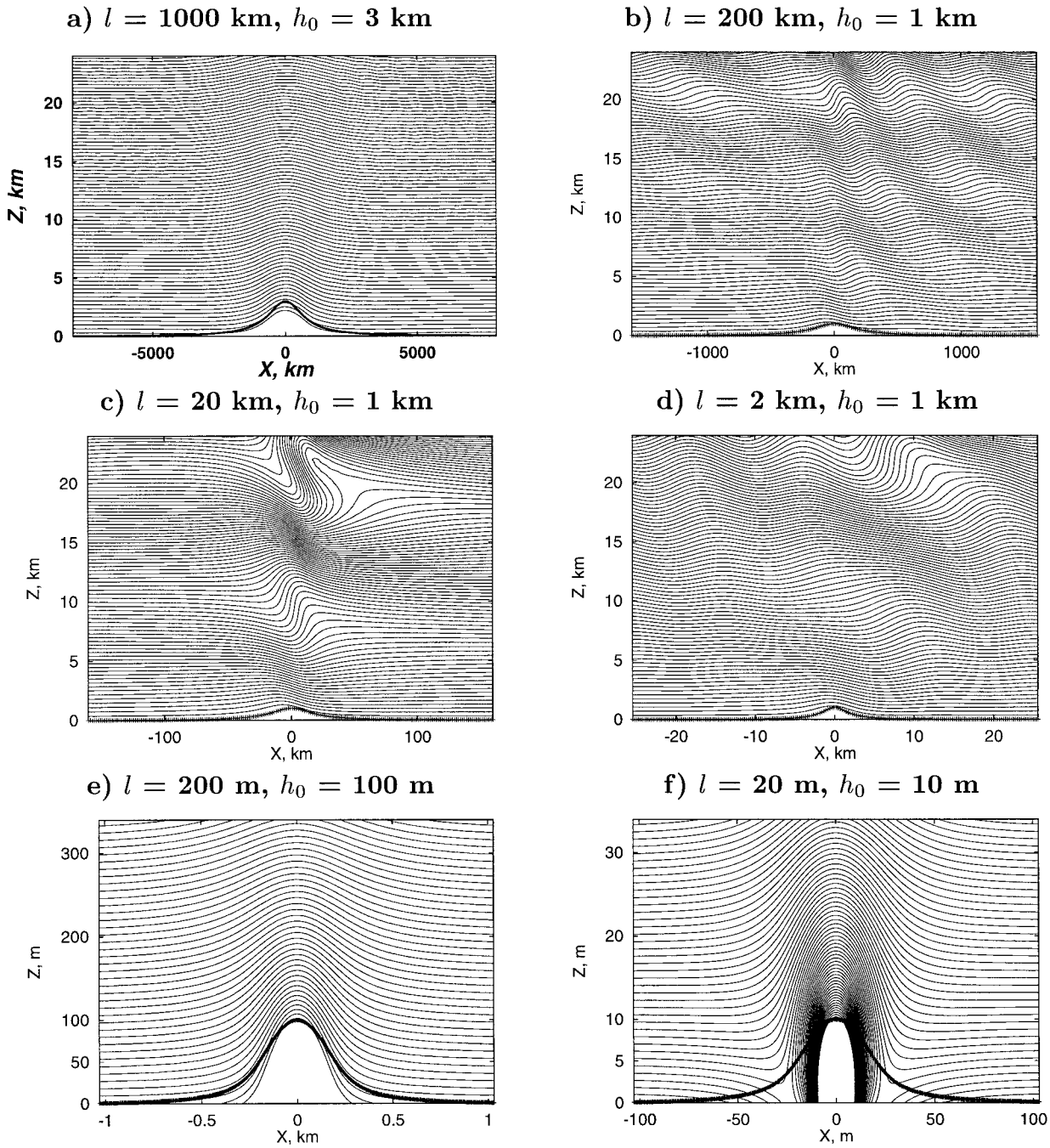

FIG. 2. Potential temperature distribution of the ExM for different l and h_0. $H_0 = 10$ km, $N = 10^{-2}$ s^{-1}, $f = 10^{-4}$ s^{-1}, and $U = 20$ m s^{-1}. Interval between Θ isolines: (a)–(d) $\Delta\Theta = 1$ *K*, (e) 0.025 *K*, and (f) 0.0025.

coincide with streamlines and intersect the mountain surface (Figs. 2a,e,f).

1) THE EFM VERSUS EXM

The first and most general conclusion, which follows from Eq. (15) and relative error behavior in Fig. 1b, is that ExM and EFM coincide for small Mach numbers. At very long orography, $l \gg c_a/f \sim 1000$ km, m_κ is indifferent to the Mach number [see (16)], and thus the EFM is a good approximation to the exact model without limitations on the Mach number there. Still, in the region $l \leq c_a/f$ the EFM differs from the ExM for large Mach numbers. This is demonstrated in Table 1 for $\mathcal{M} = 0.25$ ($U \approx 85$ m s^{-1}) and $\mathcal{M} = 0.5$ ($U \approx 170$ m s^{-1}). In Figs. 3a and 3b, potential temperature of the ExM

and potential temperature difference between EFM and ExM are presented for $\mathcal{M} = 0.25$. As seen from the table and figures, differences are small (do not exceed several percent of the wave amplitude and are almost indistinguishable in the wave pattern) if $\mathcal{M} \leq 0.25$. This condition holds for slow processes in the real atmosphere. Thus, in the case of smooth stratification, EFM can be employed for modeling of slow processes without any restriction to the spatial scale. As in this case ExM and EFM are almost indistinguishable; in future examples we will refer to them as to the single ''elastic model.'' [1]

2) ANELASTIC MODEL VERSUS ELASTIC MODEL IN THE DOMAIN OF LONG TRAPPED WAVES: $l \gg U/f \sim 100$ KM

This is the hydrostatic domain, where AEM and HSM coincide almost exactly, and thus it is relevant to treat them as the unique HSM here. Parameter m_κ has an asymptote in the case of anelastic models $\kappa \to 0$,

$$\text{HSM (AEM)}, \qquad m_\kappa \to -¼,$$

which is different from the asymptote (16) of elastic models. The asymptotic value of m_κ depends, in the case of elastic models ExM and EFM, on the stability of the atmosphere, while for the anelastic model it is independent of the stratification (see Fig. 1b). Differences in m_κ cause differences in the pattern of long trapped orographic waves. Modeling with long orography, $l = 1000$ km, is presented in Fig. 4 for background $T_0 = 280$ K, $U = 10$ m s^{-1}, and $N = 0.01$ s^{-1} (Figs. 4a,b) and $N = 0.005$ s^{-1} (Fig. 4c). Presented are the potential temperature and streamfunction patterns for two cases of the mountain height, $h_0 = 1$ and 3 km. It should be noted that an orographic pattern with characteristic half-width in synoptic scale corresponds rather to a broad upland or a system of mountain ranges (infinite in the y direction) than to the isolated mountain. In the domain of long trapped waves, the isolines of the potential temperature, as well as the streamlines, follow the orographic pattern, and there is no phase shift with the height. The spectral amplitudes of the potential temperature and streamline disturbances change with height like

$$\Theta' = \Theta_0(p)\tilde{T}'_\kappa/T_0 \sim \left(\frac{p}{p_s}\right)^{\gamma_\kappa}, \qquad \Psi'_\kappa \sim \left(\frac{p}{p_s}\right)^{\delta_\kappa},$$

where $\gamma_\kappa = -H_0N^2/g - ½ + \sqrt{-m_\kappa}$ and $\delta_\kappa = \alpha - ½ + \sqrt{-m_\kappa}$ (here $\alpha = 1$ for anelastic models). At $\kappa \to 0$, $\gamma_\kappa < 0$, whereas $\delta_\kappa > 0$. Thus, streamfunction disturbances are evanescent, whereas potential temperature fluctuations increase with height at long scales. At the same time, potential temperature and streamfunction patterns are coincident for all models at the ground. As a result, the model differences are monotonically increasing with height for Θ and they become infinite at $p \to 0$, whereas the streamfunction patterns diverge moderately, and differences are largest at the medium levels, $p/p_s \sim 0.3$–0.5.

The most sensitive field to the model choice in the long-scale region is vertical velocity w. In Fig. 5, the isolines of vertical velocity are presented for different U, l, and N in the case of high orography, $h_0 = 3$ km. As it is apparent, the differences are larger for longer scales l and moderate wind speeds U, for which m_κ is negative (left panels of Figs. 5a,b). For stronger winds ($U = 30$ m s^{-1}) or toward shorter scales, where m_κ becomes positive and free-wave pattern becomes dominant, differences between elastic and anelastic models become irrelevant. Still, small differences in the wave amplitudes are apparent down to $l = 400$ km.

The diversity of models manifests itself in relief in the long-wave compressibility. The measure of the compressibility of motion in the p space is

$$D \equiv \frac{\partial u}{\partial x} + \frac{\partial \omega}{\partial p}.$$

In the AEM model $D = 0$. In the case of the EFM the corresponding quantity is calculated from the formula

$$D = -\frac{N^2}{g}w + \frac{Q}{T_0}. \tag{17}$$

Due to the demonstrated high precision of the EFM in the long-scale domain, this formula is factually exact for D in slow dynamics and can be used in the ExM, too. As seen, D is not zero even in the absence of heat sources. The first right-hand term of (17) is approximately $10^{-5}|w|$ s^{-1}. That is, D is really very small at long scales, and its influence on the n evolution in (1e) and (6e) can be disregarded. At the same time, in the case of extremely long waves, the second, ''vertical'' term in D can be estimated as $|\partial\omega/\partial p| \sim |w|/H_0 \approx 10^{-4}|w|$, which is only 10 times the right side. That means that only 90% of the vertical term $\partial\omega/\partial p$ is balanced by the horizontal divergence $\partial u/\partial x$, and 10% remains unbalanced. Toward shorter scales, horizontal and vertical derivatives of the velocity components increase rapidly, while the right-hand term of (17) does not change much. That means that the accuracy of approximation $D = 0$ is much better for shorter scales. As shown by numerical modeling, the incompressibility condition is acceptable for all models at $l < 500$–700 km.

3) OROGRAPHIC WAVES IN THE SHORTER SYNOPTIC AND HYDROSTATIC MESOSCALE REGION: $3U/N < l \lesssim U/f$

The typical long-wave edge of the region lays at 500 km; the short-wave edge ($3U/N$) is determined by non-

[1] Still, in nonstationary numerical applications the EFM has preference, as it supports much larger (about 10 times) time stepping.

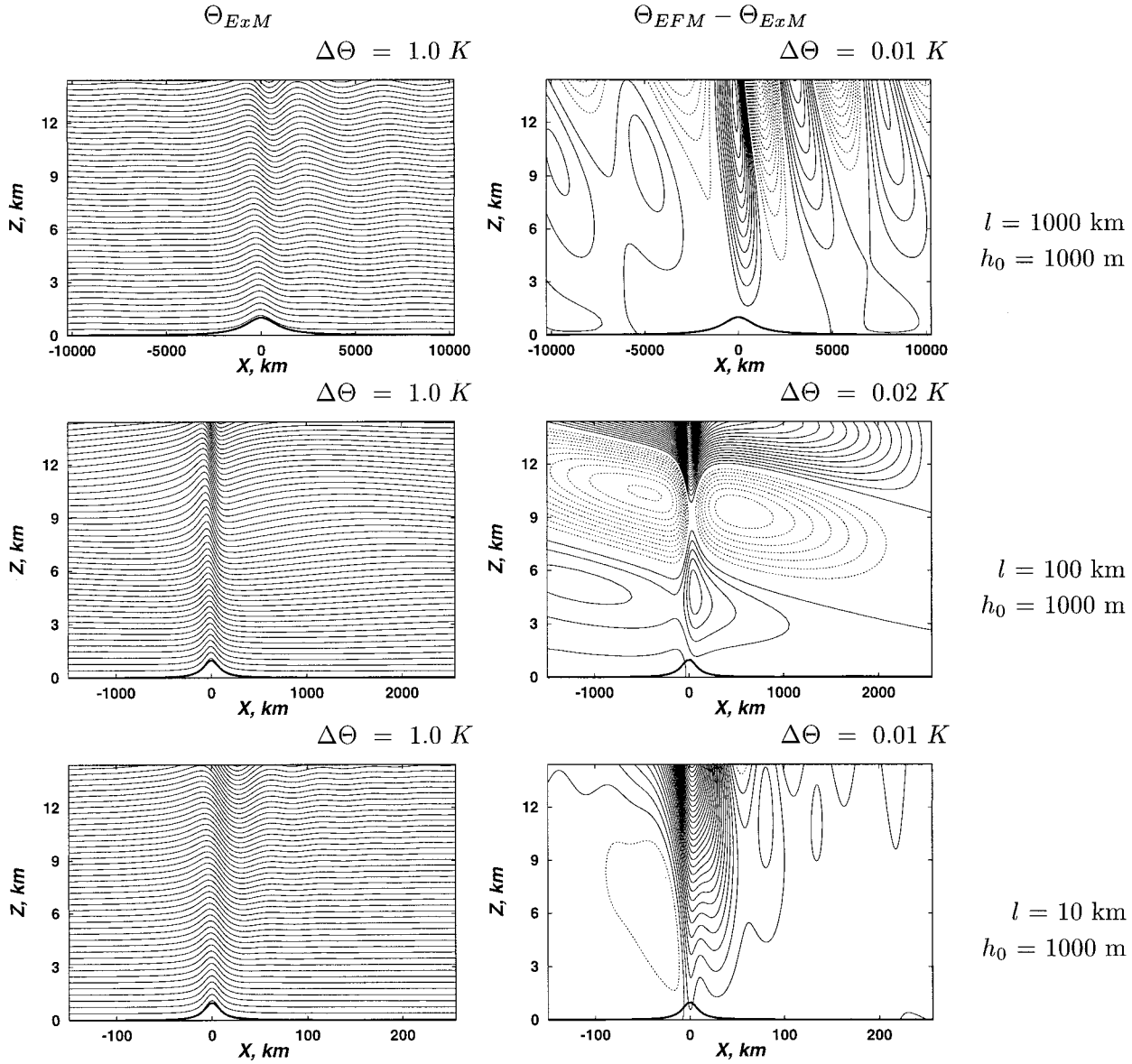

FIG. 3. Potential temperature Θ_{ExM} of ExM (left panels) and potential temperature error $\Theta_{EFM} - \Theta_{ExM}$ (right panels) of EFM at Mach number $\mathcal{M} = 0.25$, $f = 10^{-4}$ s^{-1}, $N = 10^{-2}$ s^{-1} for six sets of horizontal scale l and orographic height h_0. Dashed isolines indicate regions with negative error.

hydrostatic effects and will be considered later. This is the domain of free orographic buoyancy waves, because here $m_\kappa > 0$. As $1 - \mathcal{M}^2 + f^2/(c_a^2\kappa^2) \approx 1$ and $U^2\kappa^2 \ll N^2$ in this region, the function m_κ coincides with high accuracy for all models, satisfies condition $m_\kappa \gg 0$, and can be represented by the formula

$$m_\kappa = H_0^2\kappa^2 \times \frac{N^2}{U^2\kappa^2 - f^2}.$$

Consequently, all models behave identically with respect to w and T'. The numerical investigation reveals that streamline patterns are also coincidental for all models. As all models are here indistinguishable and ExM, EFM, and AEM coincide with the simplest representative HSM of pressure-space models, the shorter synoptic and hydrostatic mesoscale domains can be treated as the real validity region of the common HSM.

4) OROGRAPHIC WAVES IN THE NONHYDROSTATIC MESOSCALE REGION: $l < 3U/N$

Moving toward shorter scales, l enters the region where the approximation $N^2 \gg U^2\kappa^2$ does not hold. This region represents the domain where the HSM is

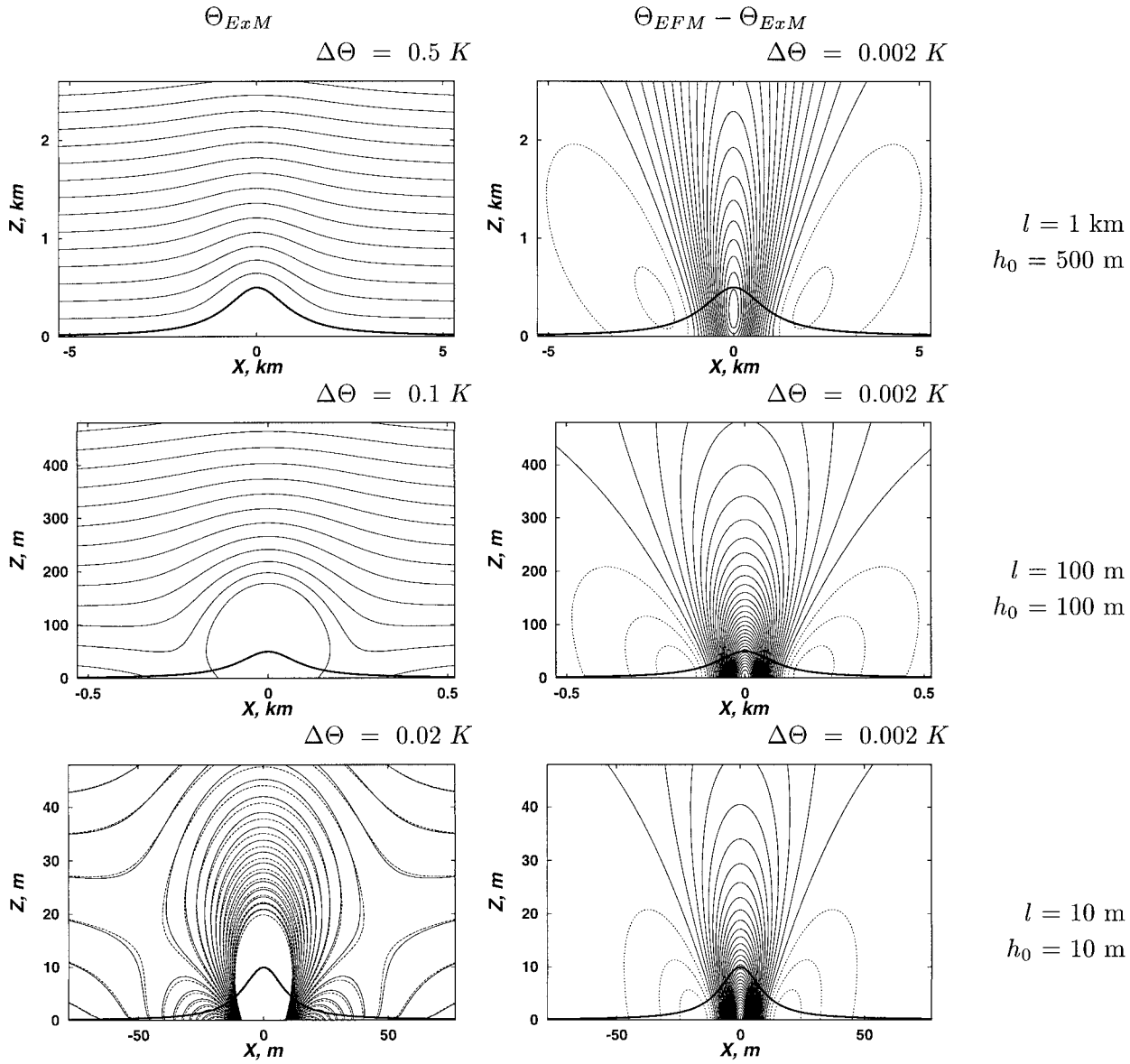

FIG. 3. (*Continued*) Dashed isolines in the bottom-left panel: EFM.

not valid, as Eq. (15d) causes systematic error. Very roughly, the long-wave border of this domain can be located at $l = H_0 \approx 10$ km. More precise estimation follows from the condition $U^2\kappa^2 > 0.1N^2$ and yields $l < 3U/N$. According to this estimation, entering the nonhydrostatic region depends essentially on the wind speed and atmospheric stability. A selection of orographically induced flow fields with $l \approx 3U/N$ is presented in Fig. 6. The ExM, EFM, and AEM, which all coincide in this domain with the highest precision and are presented as a single model, and the HSM are compared. In Figs. 6a and 6b the ''measure of the nonhydrostaticity'' $\delta =$

TABLE 1. Maximum potential temperature difference between EFM and ExM for different mountain half-widths l and Mach numbers M. Data are presented in the format Δ/ϵ, where Δ is the maximum difference in degrees kelvin in the height interval $0 \le z \le 15$ km, and ϵ represents the relative maximum difference with respect to the maximum perturbation amplitude of potential temperature.

l (m)	10	10^2	10^3	10^4	10^5	10^6
$M = 0.25$	0.0042/0.02	0.068/0.03	0.040/0.05	0.32/0.14	0.46/0.07	0.18/0.06
$M = 0.5$	1.3/0.30	1.3/0.13	0.67/0.23	0.55/0.11	0.70/0.08	0.58/0.09

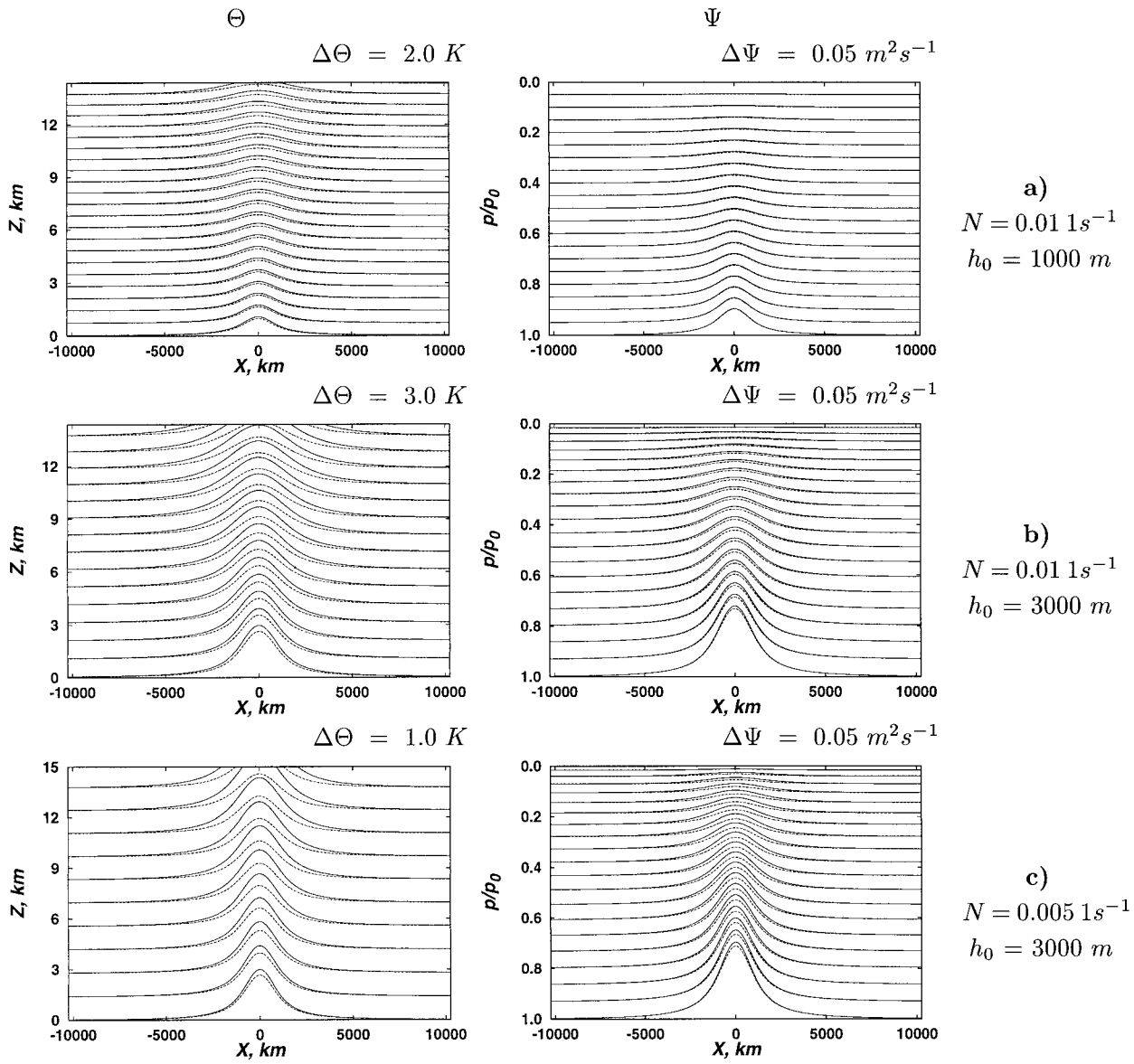

FIG. 4. Long synoptic-scale trapped orographic waves in the homogeneous background; l = 1000 km, T_0 = 280 K, $f = 10^{-4}$ s^{-1}. (left) Potential temperature isolines in common space; (right) streamfunction patterns in pressure coordinates. Continuous curves correspond to the ExM and EFM; dashed curves represent the AEM and HSM.

$3U/(Nl) = 0.9$, and the departure of the flow from hydrostatic regime is apparent, despite the characteristic horizontal scale $l = 20$ km in the first example (Fig. 6a). The comparison of flow patterns for Figs. 6a,b reveals that the departure from the HS regime increases toward shorter scales l even in the case of constant δ. Figure 6c represents differences in hydrostatic and nonhydrostatic flow patterns for the scales l deep inside the nonhydrostatic domain: $l = 3$ km, $\delta = 3$. In all examples differences grow with height and become evident first (on entering the NH domain from the long-scale edge) at upper levels of the atmosphere. Another characteristic feature, common for all examples (which was met already in the case of long waves), is that Θ disturbances are, in general, more sensitive to the model choice than Ψ disturbances. Of course, the wrong wave pattern and the inability of HSM to describe dynamics at these scales are well-known facts.

As far as the nonhydrostatic models are concerned, they are almost indistinguishable. The parameter m_κ is basically the same for all of them, except in the narrow neighborhood of the point $\kappa = N/U$, where m_κ becomes small and changes sign (which means the replacement of free waves by short trapped waves) (Fig. 1c). As

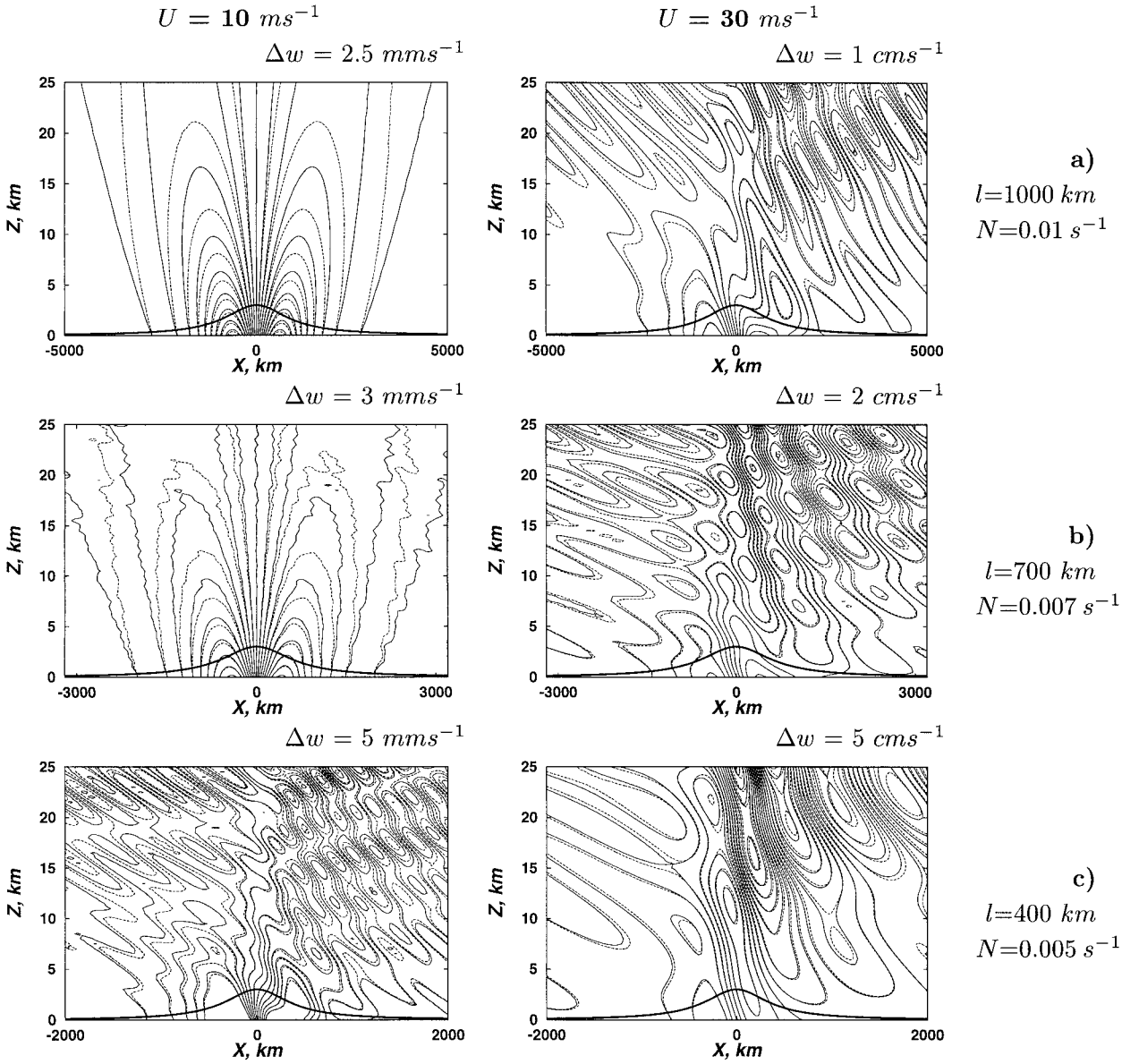

FIG. 5. Vertical velocity w for different l and N combinations in the case of medium wind, $U = 10$ m s^{-1}, and strong wind, $U = 30$ m s^{-1}. Continuous curves, ExM and EFM; dashed curves, AEM and HSM.

numerical modeling shows, these differences are of no visible consequence to the flow patterns.

5) OROGRAPHIC WAVES IN THE MICROSCALE DOMAIN: $l < 10U^2/g$

Moving toward shorter scales, one enters the domain (begins almost immediately with $l < N/U$), where (15) simplifies for all NH models (assuming $\mathcal{M} \ll 1$) to

$$m_\kappa = -(H_0\kappa)^2.$$

As a consequence, the ExM, AEM, and EFM are identical with respect to the vertical displacement and vertical velocity description. The flow is in the highest degree incompressible in the p space; that is, $D = 0$, in this domain for all models, and the streamfunctions of EFM and AEM yield coinciding streamlines. This follows from Eq. (13), which for small-scale near-ground processes with $(p/p_s)^{1-\alpha} \approx 1$ yields a velocity field, which is coincidental with the AEM. Thus, in dynamical respect the flow in microscale domain is incompressible in the p space in the highest degree and the AEM is valid along with other models for describing the flow pattern. This microscale identity of vertical

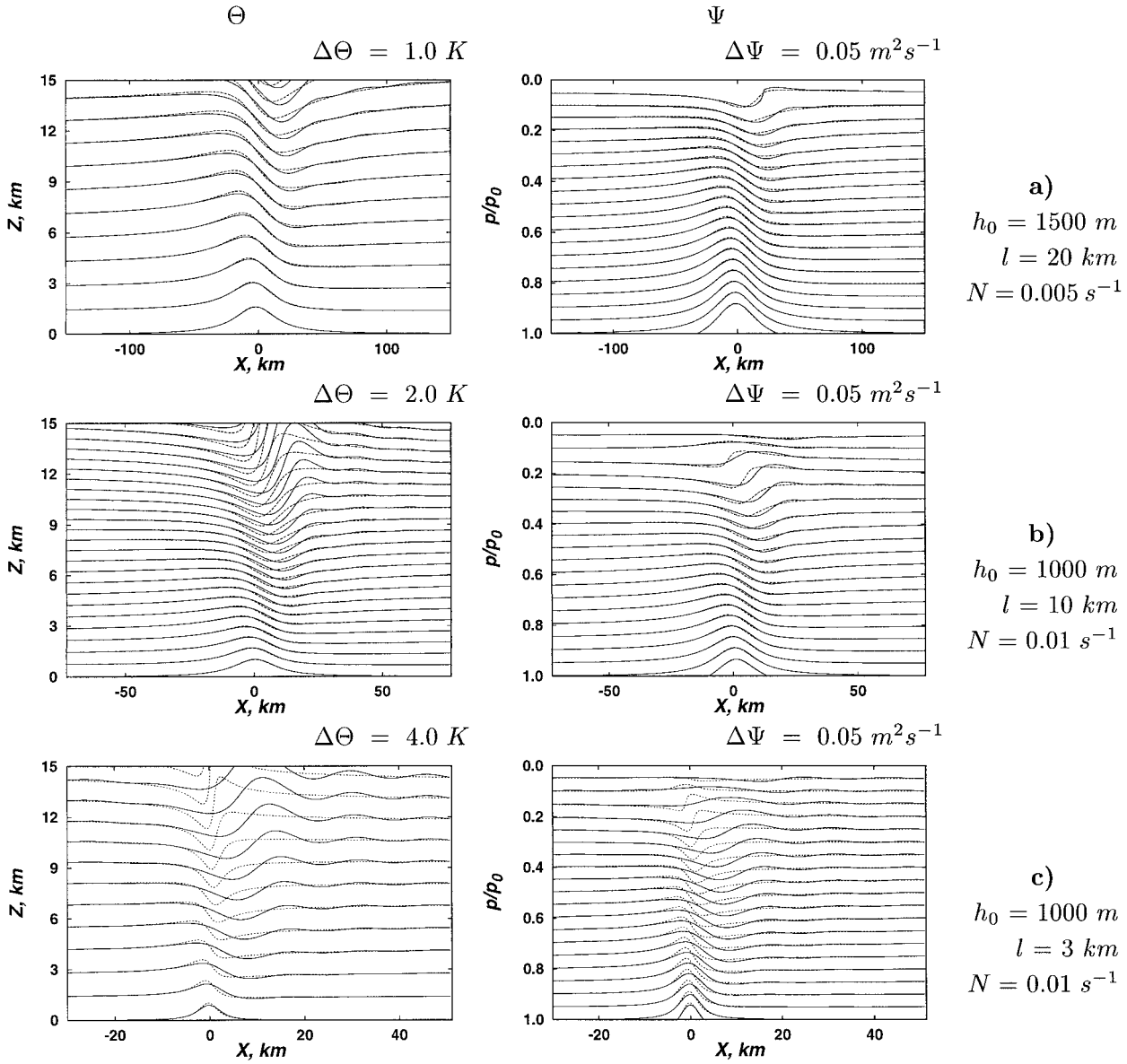

FIG. 6. Comparison of potential temperature and streamfunction patterns of the ExM, EFM, and AEM (continuous curves) and HSM (dotted curves) in the domain of the transition from hydrostatic regime (a) to the nonhydrostatic flow (b), (c); $U = 30$ m s^{-1}.

velocity and streamline pattern for different models is not restricted to shorter scales, and the streamline field looks, for instance, in deep microscale $1/\kappa = 1$ m, exactly the same for all NH models.

Nevertheless, the similarity of these models is not a general feature of microscale. At very short scales, thermodynamic reaction of the atmosphere becomes different again. The largest diversity is exhibited by the temperature fluctuation field. The general expression for the spectral amplitude of the temperature fluctuation reads (Rõõm 1997)

$$\frac{\tilde{T}'_\kappa(p)}{T_0} = -(1 + d_\kappa)\frac{N^2}{g}a_\kappa,$$

where

$$d_\kappa = \begin{cases} 0 & \text{for AEM} \\ \dfrac{H_0}{g}\dfrac{\kappa^2U^2 - N^2}{1/2 - \alpha + \sqrt{-m_\kappa}} \approx \dfrac{U^2\kappa}{g} & \text{for ExM and EFM.} \end{cases}$$

Departure of the AEM from elastic models ExM and EFM becomes apparent for $d_k > 0.1$, which yields $l <$

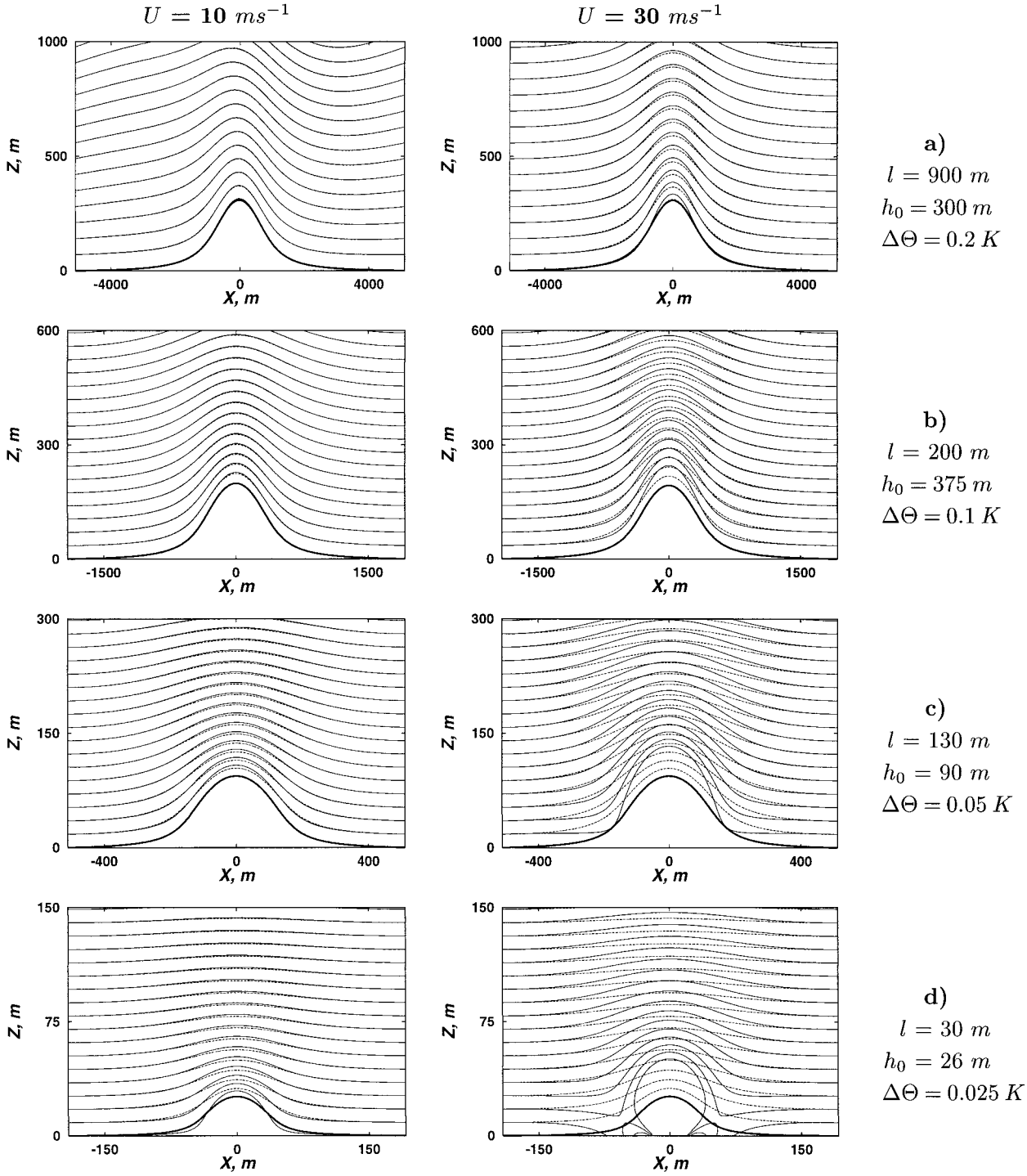

FIG. 7. Potential temperature Θ distribution in the case of medium wind, $U = 10$ m s^{-1} (left) and strong wind, $U = 30$ m s^{-1} (right) in the shorter mesoscale and microscale domains; $N = 0.01$ s^{-1}. Continuous curves, ExM and EFM; dashed curves, AEM.

$10U^2/g$ (which is approximately 100 m for moderate winds and 1000 m for strong winds). This is the region where the AEM model becomes erroneous in describing temperature fluctuations. The transformation of the temperature field from shorter mesoscale ($l \sim 1000$ m) to microscale ($l \sim 50$ m) is demonstrated in Fig. 7. The climatologically mean stratification with $N = 0.01$ s^{-1} is employed. As evident, the departure of the AEM

from the ExM is much more significant for strong winds ($U = 30$ m s^{-1}) and becomes evident already at $l = 900$ m, while in the case of moderate winds the AEM is valid satisfactorily even at $l = 30$ m. The temperature depression for elastic models near the hilltop is much larger than for the AEM. The difference can reach ~0.2 K at $l = 200$ m and shorter. Such differences are not essential for dynamical flow pattern but can be significant for microphysical processes related to water phase transitions and in thermal convection.

4. On the effect of the atmospheric inhomogeneity on the model diversity

All the obtained results and deduced estimates assume a homogeneous background flow with constant H_0 and N. The problem arises whether inhomogeneity of the atmosphere can add some new principal effects that could enhance the observed diversity of models. One could get involved to the minutest detail of this question. Still, a qualitative examination of the situation with a temperature jump at a single isolated level, p_*, should give a comprehensive answer, because the finite temperature jump (or its equivalent, the scale-height jump) represents the ultimate example of a nonhomogeneous background.

A jump in the scale height,

$$H_0(p) = H_-, \qquad p < p_*,$$
$$H_0(p) = H_+ < H_-, \qquad p > p_*, \tag{18}$$

where H_- and H_+ are constants, generates the δ singularity in buoyancy frequency N at the level p_*:

$$N^2 = N_0^2(p) + N_1^2\,\delta(p - p_*),$$

where

$$N_0^2 = gR/(C_p H_-), \qquad p < p_*,$$
$$N_0^2 = gR/(C_p H_+), \qquad p > p_*,$$
$$N_1^2 = -\frac{g p_* \Delta H}{\overline{H}^2}, \quad \overline{H} = (H_- + H_+)/2, \quad \Delta H = H_+ - H_-.$$

[We have used the exact dependence of N on H_0, Eq. (5).] As N and H_0 are constants above and below the surface p_*, characteristics of different models are similar to those of models in the homogeneous atmosphere in subdomains $p < p_*$ and $p > p_*$. New unexpected qualities, if any, should become apparent at the surface p_*. This is the surface of the discontinuity of the medium and here the refraction and reflection of buoyancy waves are the only physical effects of relevance.

The wave breaking at level p_* is governed by the behavior of displacement amplitude a. Because the operator $\hat{M}$ in Eq. (7a) includes δ singularities in coefficients, the second derivative of the displacement is singular and its first derivative has a finite jump at p_*. A closer study of Eq. (7a) reveals that, in the case of elastic models ExM and EFM, the displacement amplitude a is continuous, whereas its first derivative has a finite jump at p_*. For the Fourier amplitude $\tilde{a}_\kappa$ these conditions are

$$\text{ExM, EFM,} \quad \Delta(\tilde{a}_\kappa) = 0, \tag{19a}$$

$$\Delta\left(\frac{1}{H_0^2}\frac{\partial \tilde{a}_\kappa}{\partial p}\right) = \left\{\frac{g\kappa^2 \Delta H_0}{\overline{U}^2\kappa^2 - f^2}\overline{\left(\frac{1}{H_0^2}\right)} - \alpha\left[\Delta H_0 \overline{\left(\frac{1}{H_0^3}\right)} + \Delta\left(\frac{1}{H_0^2}\right)\right]\right\}\frac{\overline{\tilde{a}_\kappa}}{p_*}, \tag{19b}$$

where $\Delta(\cdot)$ and $\overline{(\cdot)}$ denote the jump and mean value of a function at p_*:

$$\Delta(\phi) = \phi(p_* +) - \phi(p_* -),$$
$$\overline{(\phi)} = \frac{1}{2}[\phi(p_* -) + \phi(p_* +)].$$

According to Eq. (7b), the same conditions hold for w. Thus, $w_- = w_+$ in the case of elastic models; that is, the medium is continuous in the common space.

As reveals inspection of Eq. (7a) with operators (8c) and (8d) in the case of anelastic models, continuous at the discontinuity level must be rather the function a/H_0, and analogues of conditions (19a) and (19b) are

$$\text{AEM, HSM,} \quad \Delta\left(\frac{\tilde{a}_\kappa}{H_0}\right) = 0, \tag{20a}$$

$$\Delta\left(\frac{\partial}{\partial p}\frac{\tilde{a}_\kappa}{H_0}\right) = \frac{g\kappa^2 \Delta H_0}{p_*(\overline{U}^2 k^2 - f^2)}\overline{\left(\frac{\tilde{a}_\kappa}{H_0}\right)}. \tag{20b}$$

In the linear case, when (2a) reduces to $w = H_0\omega/p$, the relationship $\omega/p = w/H_0 = d_0(a/H_0)/dt$ holds in accordance with (7b). Thus, the first condition here states that in the case of anelastic models the omega velocity is continuous at p_*; that is, the medium is rather continuous in the pressure-space.

Equations (19) and (20) represent exact boundary conditions for a at p_*, which permit the solution to continue from one side of the temperature discontinuity surface to the other side.

As seen from (19) and (20), the solution of the wave equation behaves differently for elastic and anelastic models at discontinuity surfaces of the temperature. Thus, wave breaking and reflection are different for these two groups of models in general. Still, as it reveals, differences are small and negligible in the majority of cases of practical relevance if the temperature jump is small, $|\Delta H| \ll \overline{H_0}$. In this case, jumps in a (if any) and in $\partial a/\partial p$ are small, and general discontinuity conditions (19) and (20) can be essentially simplified with the help of relations $\overline{(H_0^n)} \approx \overline{H_0}^n$, $\Delta(H_0^n) \approx n\overline{H_0}^{n-1}\Delta H_0$, and $\Delta(ab) \approx \overline{a}\Delta b + \overline{b}\Delta a$ (valid if $|\Delta a| \ll |\overline{a}|$ and $|\Delta b| \ll |\overline{b}|$):

$$\text{ExM, EFM,} \quad \Delta(\tilde{a}_\kappa) = 0, \tag{21a}$$

$$\Delta\left(\frac{\partial \tilde{a}_\kappa}{\partial p}\right) \approx \frac{\Delta H_0}{\overline{H_0}}\left[\left(\frac{\overline{C_0}^2 k^2}{\overline{U}^2 k^2 - f^2} + \alpha\right)\frac{\overline{\tilde{a}_\kappa}}{p_*} + 2\overline{\left(\frac{\partial \tilde{a}_\kappa}{\partial p}\right)}\right]; \tag{21b}$$

$$\text{AEM, HSM,} \quad \frac{\Delta \tilde{a}_\kappa}{\tilde{a}_\kappa} = -\frac{\Delta H_0}{\overline{H_0}} \tag{22a}$$

$$\Delta\left(\frac{\partial \tilde{a}_\kappa}{\partial p}\right) \approx \frac{\Delta H_0}{\overline{H_0}}\left[\left(\frac{\overline{C_0}^2 k^2}{\overline{U}^2 k^2 - f^2} + \beta\right)\frac{\overline{\tilde{a}_\kappa}}{p_*} + \overline{\left(\frac{\partial \tilde{a}_\kappa}{\partial p}\right)}\right], \tag{22b}$$

where $C_0 = \sqrt{gH_0} \approx 280$ m s^{-1}; and

$$\beta = -p_* \overline{H_0}\frac{\Delta(\partial \ln H_0/\partial p)}{\Delta H_0} \approx p_*\left[\frac{\overline{(\partial H_0/\partial p)}}{\overline{H_0}} - \frac{\Delta(\partial H_0/\partial p)}{\Delta H_0}\right].$$

As seen from (22a), discontinuity of the displacement amplitude is always small in anelastic models, and, as a first approximation, a can be considered as continuous. The same is true for the jump of the derivative, $\Delta(\partial \tilde{a}_\kappa/\partial p)$, in all models if terms in square brackets on the right sides of (21b) and (22b) are small (~ 1 or $\ll 1$). In such circumstances $|\Delta(\partial \tilde{a}_\kappa/\partial p)| \ll |\overline{\tilde{a}_\kappa/p_*}|$, and there is no significant wave refraction or reflection at all. The wave breaking becomes relevant if some of the terms in square brackets become large. In the principal plane, the right sides of (21b) and (22b) can gain a large contribution from terms $\overline{C_0}^2\kappa^2/(\overline{U}^2\kappa^2 - f^2)$ ($\sim \overline{C_0}^2/\overline{U}^2 \gg 1$ for scales $l \sim 1/\kappa < 1000$ km), $\overline{(\partial \tilde{a}_\kappa/\partial p)}$, and, in the case of anelastic models, from the term with β. Still, in the realistic atmospheric conditions, $\overline{(\partial \tilde{a}_\kappa/\partial p)} \sim \overline{\tilde{a}_\kappa}/p_*$ and $|\beta| < 1$ {in particular, $\beta = 0$ in the model atmosphere [(18)]}. In such circumstances, Eqs. (21b) and (22b) can be simplified to identical appearance:

$$\Delta\left(\frac{\partial \tilde{a}_\kappa}{\partial p}\right) = \frac{\overline{\tilde{a}_\kappa}}{p_*}\frac{\Delta H}{\overline{H}}\frac{C_0^2\kappa^2}{\overline{U}^2\kappa^2 - f^2}.$$

Thus, excluding the very specific situations with large β, or very large vertical gradients of a in the neighborhood of the level p_*, the wave breaking at temperature discontinuities is essential in the scale domain $l < 1000$ km, where it is indistinguishable for elastic and anelastic models.

5. Conclusions

Obtained results can be summarized as follows.

1) The EFM coincides with the ExM in the description of slow processes everywhere, without restrictions to the spatial scales. If there is any restriction with respect to this model, it is the uncertainty in its quality while describing strongly nonlinear advection and convection, as there has been no numerical or analytical study using the EFM in this field as of yet. Still, model experiments with uniform background advection show the quality of the model at linear and moderately nonlinear flows.
2) The AEM is defective in the long-scale domain, $l \sim$ 1000 km and larger. It disregards the long-scale compressibility, which is different from zero according to (17), and it yields observable error in the entropy and vertical velocity distributions. Because the AEM coincides in the long-scale limit with the HSM, this defect is common to all hydrostatic primitive equation models. To get significant observable differences between the models, we employed ultimate conditions, particularly the large mountain height ($h_0 =$ 3 km). Still, the differences in modeled fields are not caused by large orography but by differences in function m_κ (15) in the long-scale domain, that is, by inherent differences in models. The large mountain heights were necessary to get large amplitudes of modeled fields. Thus, differences in AEM and ExM should be of the same order in all instances where the spatial scales and amplitudes of processes are similar to the ones used in the experiments above: $l_x \sim l \sim 1000$ km, $l_z \sim h_0 \sim 3$ km, $U \sim$ 10–30 m s^{-1}, $w \sim 1$ cm s^{-1}. These values are typical in a mature cyclone. Meanwhile, it is not clear how important this error is for real synoptic-scale evolution. The effect lies in the scales that are longer than the domain of maximum baroclinic instability. Also, the described departure in w and Θ fields becomes evident at large heights, in the upper troposphere and tropopause, as it grows cumulatively with the height. Therefore, further numerical experiments on cyclogenesis are required to obtain a final answer.
3) Beginning with $l \sim$ 500–700 km and shorter scales, the atmosphere becomes anelastic (nondivergent) in the p space for slow processes with the highest degree of accuracy. This is the domain where all three NH models, ExM, EFM, and AEM, are coincidental. Still, the preferred model is AEM due to its simplicity. The domain of incompressibility is not restricted at the short-scale end, and, as a consequence, the dynamical flow pattern is described by AEM adequately down to scales ~1–10 m. Still, the thermodynamic adequacy of the model is poor below 1000 m, and errors in temperature field may reach 0.1–0.2 K near the ground. Errors of the same order are expected in local thermal convection. Whether or not this is a meaningful deviation depends on the problem. For mechanical flow and accompanying material transport, small errors in temperature field are irrelevant, but this is not the case for thermal convection and moist thermodynamic processes. Anyway, when the exactness of the thermodynamic fluctuations is required, preference should be given to the EFM in the microscale domain $l < 10U^2/g <$ 1000 m.
4) The wave breaking and reflection at moderate temperature discontinuities, $\Delta T_0 \ll T_0$, is either (in the long-scale region, $l > 1000$ km) unimportant, or (in the domain $l < 1000$ km) it is identical for all pressure-space models: ExM, EFM, AEM, and HSM.

Consequently, the changing stratification of the atmosphere, and particularly jumps in temperature distributions, do not cause different physical effects for different *p*-space models. All conclusions about the quality of EFM, AEM, and HSM, formulated for homogeneous background, remain valid for optional stratification.

Acknowledgments. This investigation has been supported by the Estonian Science Foundation under Grant 2624.

REFERENCES

Alaka, M. A., Ed., 1960: The airflow over mountains. WMO Tech. Rep. 34, 135 pp.

Baines, P. G., 1995: *Topographic Effects in Stratified Flows.* Cambridge University Press, 482 pp.

Bubnova, R., G. Hello, P. Benard, and J. F. Geleyn, 1995: Integration of the fully elastic equations cast in the hydrostatic pressure terrain-following coordinate in the framework of the ARPEGE/Aladin NWP system. *Mon. Wea. Rev.,* **123,** 515–535.

Eliassen, A. 1949: The quasi-static equations of motion with pressure as independent variable. *Geofys. Publ. (Oslo),* **17** (3), 44 pp.

Hereil, Ph., and R. Laprise, 1996: Sensitivity of internal gravity waves solutions to the time step of a semi-implicit semi-Lagrangian nonhydrostatic model. *Mon. Wea. Rev.,* **124,** 972–999.

Holton, J. R., 1992: *An Introduction to Dynamic Meteorology.* 3d ed. Academic Press, 511 pp.

Laprise, R., 1992: The Euler equations of motion with hydrostatic pressure as an independent variable. *Mon. Wea. Rev.,* **120,** 197–207.

——, and W. R. Peltier, 1989: On the structural characteristics of steady finite-amplitude mountain waves over bell-shaped topography. *J. Atmos. Sci.,* **46,** 586–595.

Lin, Y.-L., and T.-A. Wang, 1996: Flow regimes and transient dynamics of two-dimensional stratified flow over an isolated mountain ridge. *J. Atmos. Sci.,* **53,** 139–158.

Long, R. R., 1953: Some aspects of the flow of stratified fluids. Part I: A theoretical investigation. *Tellus,* **5,** 42–58.

Miller, M. J., and R. P. Pearce, 1974: A three-dimensional primitive equation model of cumulonimbus convection. *Quart. J. Roy. Meteor. Soc.,* **100,** 133–154.

Miranda, P. M. A., and I. N. James, 1992: Non-linear three-dimensional effects on gravity-wave drag: Splitting flow and breaking waves. *Quart. J. Roy. Meteor. Soc.,* **118,** 1057–1081.

——, and M. A. Valente, 1997: Critical level resonance in three-dimensional flow past isolated mountains. *J. Atmos. Sci.,* **54,** 1574–1588.

Nance, L. B., and D. R. Durran, 1994: A comparison of the accuracy of three anelastic systems and the pseudo-incompressible system. *J. Atmos. Sci.,* **51,** 3549–3565.

Queney, P., 1948: The problem of airflow over mountains: A summary of theoretical studies. *Bull. Amer. Meteor. Soc.,* **29,** 16–26.

Rõõm, R., 1989: The general form of dynamical equations of the atmosphere in the isobaric coordinate space. *Proc. Est. Acad. Sci., Phys., Math.,* **38,** 368–371.

——, 1990: General form of the dynamical equations for the ideal atmosphere in the isobaric coordinate system. *Izv. SSSR, Fiz. Atmos. Okeana,* **26,** 17–26.

——, 1997: Nonhydrostatic atmospheric dynamics in pressure-related coordinates. Tech. Rep., Estonian Science Foundation Grant 172, Tartu Observatory, 105 pp.

——, 1998: Acoustic filtering in nonhydrostatic pressure coordinate dynamics: A variational approach. *J. Atmos. Sci.,* **55,** 654–668.

——, and A. Ülejõe, 1996: Nonhydrostatic acoustically filtered equations of atmospheric dynamics in pressure coordinates. *Proc. Est. Acad. Sci., Phys., Math.,* **45,** 421–429.

Salmon, R., and L. M. Smith, 1994: Hamiltonian derivation of the nonhydrostatic pressure-coordinate model. *Quart. J. Roy. Meteor. Soc.,* **120,** 1409–1413.

Scorer, R. S., 1949: Theory of waves in the lee of mountains. *Quart. J. Roy. Meteor. Soc.,* **75,** 41–56.

——, 1953: Theory of airflow over mountains: II—The flow over a ridge. *Quart. J. Roy. Meteor. Soc.,* **79,** 70–83.

——, 1954: Theory of airflow over mountains: III—Airstream characteristics. *Quart. J. Roy. Meteor. Soc.,* **80,** 417–428.

——, 1956: Airflow over an isolated hill. *Quart. J. Roy. Meteor. Soc.,* **82,** 75–81.

Smith, R. B., 1979: The influence of mountains on the atmosphere. *Advances in Geophysics,* Vol. 21, Academic Press, 87–230.

White, A. A., 1989: An extended version of nonhydrostatic, pressure coordinate model. *Quart. J. Roy. Meteor. Soc.,* **115,** 1243–1251.

Xue, M., and A. J. Thorpe, 1991: A mesoscale numerical model using the nonhydrostatic pressure-based sigma-coordinate equations: Model experiments with dry mountain flows. *Mon. Wea. Rev.,* **119,** 1168–1185.